



Characterisation of damage mechanisms in oxide ceramics indented at dynamic and quasi-static strain rates



C.E.J. Dancer^{a,b,*}, J.N.F. Spawton^a, S. Falco^c, N. Petrinic^c, R.I. Todd^a

^a Department of Materials, University of Oxford, Parks Road, Oxford, OX1 3PH, UK

^b International Institute for Nanocomposite Manufacturing, Warwick Manufacturing Group, University of Warwick, Gibbet Hill, Coventry, CV4 7AL, UK

^c Department of Engineering Science, University of Oxford, Parks Road, Oxford, OX1 3PJ, UK

ARTICLE INFO

Keywords:

Armour

Al₂O₃

ZrO₂

Mechanical properties

Residual stress

ABSTRACT

Ceramic materials are known to display rate dependent behaviour under impact. Tests to establish the strain-rate dependent variations in damage mechanisms have been carried out on debased alumina, an alumina-zirconia composite, and 3Y-TZP. Materials were indented dynamically and quasi-statically using identical sharp hardened steel projectiles while recording the load profile. Characteristics typical of both sharp and blunt indentation types were observed using scanning electron microscopy and piezospectroscopic mapping. At dynamic strain rates both the depth of the indentation and the residual stress in the material were lower than for quasi-static tests. This was attributed to temperature-induced softening of the projectile. Unusual behaviour was observed in the 3Y-TZP samples due to the reversible transformation from tetragonal to monoclinic crystal structures during mechanical loading. These effects and the observed superior mechanical strength against impact suggest that zirconia or zirconia-composite materials may have advantages over debased alumina for application as ceramic armour materials.

1. Introduction

Ceramic materials are both strong under compressive loads and extremely hard [1], and therefore have excellent resistance to indentation. This, combined with other properties such as their low density and resistance to wear, means they are attractive for use in armour systems [2–4]. Ceramics exhibit strain rate-dependent mechanical behaviour above some critical strain rate, which has been determined as *ca.* 10²–10³ s^{−1} for both polycrystalline alumina and silicon carbide [5,6]. This strain rate-dependent behaviour is one of the reasons why the performance of ceramic materials impacted at high strain rates (e.g. ballistic velocities) is not related in a straightforward way to their mechanical properties as measured at quasi-static low strain rates [7,8]. This is because the sequence of fracture mechanisms occurring in ceramic materials during dynamic testing is known to differ from that in quasi-static testing [9–13].

Ballistic testing involves high velocity (> 700–800 m/s) impact of a sphere, rod or sharpened bullet, sometimes encased in a metal sheath, on relatively large ceramic discs or tiles [14,15]. Such testing, while effective at establishing a qualitative relative performance of material compositions against the specific threat tested [8], will typically result

in a high degree of destruction of the ceramic material. This severely limits the ability of post-test characterisation to establish the micro-mechanisms occurring which lead to failure. It is therefore difficult to develop physically based models for impact and to understand how the microstructure of the material should be modified to manufacture a material with greater resistance to damage [16,17]. Due to the limited microstructural information which can be obtained from ballistic testing, in our previous study [12] a test was developed which was carried out at sub-ballistic speeds on alumina samples using smaller projectiles designed to resemble real armour-piercing bullet cores. The sub-ballistic impact velocities allow a greater number of samples to be recovered in an essentially intact state, and therefore post-testing measurement of residual stress and some quantification of the degree of deformation of the impacted surface could be carried out and compared to analytical models [11,12]. At the same time, the projectile is sharp, so the strain-rate at the point of impact is locally very high and so gives information relevant in more energetic impacts.

A dynamic indentation hardness tester using a diamond Vickers hardness indenter mounted in a split Hopkinson pressure bar has previously been developed and used to test a number of materials by Subhash and coworkers [18–20]. However our setup has a number of

* Corresponding author at: International Institute for Nanocomposite Manufacturing, Warwick Manufacturing Group, University of Warwick, Gibbet Hill, Coventry, CV4 7AL, UK

E-mail address: c.dancer@warwick.ac.uk (C.E.J. Dancer).

<https://doi.org/10.1016/j.jeurceramsoc.2019.06.054>

Received 26 March 2019; Received in revised form 27 June 2019; Accepted 28 June 2019

Available online 02 July 2019

0955-2219/ © 2019 The Authors. Published by Elsevier Ltd. This is an open access article under the CC BY license (<http://creativecommons.org/licenses/by/4.0/>).

advantages as an analogue for a ballistic test. First, by using a projectile rather than a diamond-tipped hardness indenter we can study the effect of impact on the projectile as well as on the target, rather than indenting with such a rigid hard material that the indenter is unaffected. Secondly, by using a gas-gun to propel the projectile rather than the split Hopkinson pressure bar, higher strain rates are attained during impact. Koepfel and Subhash [18] defined the strain rate in their dynamic hardness tests as the ratio of the indenter velocity to the size of the indentation. The maximum strain rate in our test occurs on initial impact, when the velocity is highest and the projectile is still sharp. By dividing typical values for the impact velocity and by those for the indentation diameter in our test we calculate a maximum strain rate of $1 \times 10^5 \text{ s}^{-1}$; in comparison the dynamic hardness tester achieves a strain rate of $2.2 \times 10^3 \text{ s}^{-1}$ [18]. This means the strain rate in our dynamic test lies comfortably in the dynamic regime rather than in the region of the static-dynamic transition mentioned above. This will result in our setup allowing a more reliable comparison to ballistic tests and a greater contrast when compared with quasi-static indentations.

Silicon carbide, alumina and boron carbide are currently the most widely used armour ceramics [2,4,15]. While boron carbide and silicon carbide have superior performance against ballistic threats compared to alumina, their high temperature processing requirements mean they are significantly more expensive to produce [1,16]. Compared to alumina, tetragonal zirconia polycrystals (TZP) have a higher toughness which is known to be an important property for armour applications [2]. The enhanced toughness is due to the fact that TZP undergoes a phase transition from tetragonal to monoclinic when under an applied tensile stress [21–23]. The volume expansion (ca. 4%) which occurs when this transition occurs due to the tensile stress at a crack tip results in a compressive stress, which limits crack growth [22,24]. The toughness of TZP is therefore higher than that of other ceramics such as alumina, where this transition does not occur. However the typical density of 6.10 g/cm^3 for yttria-stabilised TZP is significantly higher compared with alumina (3.96 g/cm^3) and with carbide materials such as boron carbide (2.52 g/cm^3) and silicon carbide (3.21 g/cm^3), which makes it less attractive for armour applications where weight is generally an important factor [1]. However if superior performance were obtained for the TZP, it may prove possible to use comparatively thinner plates of TZP which would save reduce the weight and mitigate the disadvantage of the higher density. In addition, it is reasonable to suggest that a composite material containing TZP may offer a good compromise between the superior toughness of TZP and the lower density and higher hardness of alumina, or one of the carbide materials.

In this work, we extend our previously-described dynamic test [11,12] developed for alumina to study impact and indentation of both a composite zirconia-alumina material and 3Y-TZP, and compare their behaviour to that of debase polycrystalline alumina tested under identical conditions. In addition we determine the effect on the degree of damage sustained by reducing the impact speed to quasi-static rates for these ceramic materials.

2. Experimental methods

Three oxide ceramic materials sintered from mixed oxide powders

were obtained in the form of large discs of 100–120 mm diameter and 8 mm thickness. The materials were debase alumina (95 wt% alumina with a glassy phase formed from multiple oxide additions), a composite zirconia-alumina material (90 wt% alumina, 10 wt% stabilised zirconia), and tetragonal zirconia polycrystals (3Y-TZP) (94 wt% zirconia, 5.4 wt% yttria, 0.25 wt% alumina). To obtain suitable materials for impact tests, discs of approximately 25 mm diameter were drilled from the as-supplied material using a diamond-coated core drill (DK Holdings, UK). Samples were flat-bed ground (Jones & Shipman, UK) on both sides to ensure parallelism, and to obtain a suitable surface for subsequent microscopic examination the surface to be impacted or indented was polished to a $3 \mu\text{m}$ finish using diamond pastes.

Samples of suitable dimensions for other characterisation methods were cut from the as-supplied discs using a diamond blade and polished to a $1 \mu\text{m}$ finish except where stated otherwise. The bulk density was measured using Archimedes' method with water as the immersion medium. Hardness indentations were made using a Vickers hardness indenter (Vickers-Armstrong, UK) with a 10 kg load, and the dimensions of the indentations were determined using an optical confocal microscope (InfiniteFocus Optical Microscope, Alicona, Austria) with a 20x objective lens. The fracture strength was determined by 4-point bending tests using eight samples per material, using a jig which conformed to British Standard EN 843-1:2006 [25]. The Young's modulus, shear modulus, and Poisson's ratio were calculated from measured resonance frequencies determined using as-supplied discs by the impulse resonance technique (Grindosonic, J.W. Lemmens N.V, Leuven, Belgium) following the methods given in British Standard EN 843-2:2006 [26]. The grain sizes of the materials were determined by the linear intercept method described by Mendelson [27] using SEM micrographs of specimens which were polished to $0.25 \mu\text{m}$ finish, thermally etched in air, and coated with 2 nm of platinum. A multiplication factor of 1.56 was applied to convert the 2D projections to the expected 3D sizes [27].

The projectiles used in all tests were manufactured in house from hardened tool steel. This material was chosen for its ability to inflict measurable damage on the ceramic materials without shattering during testing. 3 mm diameter centreless-ground silver steel rods (composition BS-1407) were heated to 760°C at a rate of 15°C/min , held for 20 min and quenched in a water bath. The resulting material had a Vickers hardness of 8.6 GPa measured on a cross-sectional slice through one of the rods. To make each projectile, a hardened steel rod was sharpened using a cooled diamond wheel and then sectioned at a suitable length using a cubic boron nitride blade. The cut surface of the projectile was ground using a flatbed grinder to ensure flat, perpendicular bases. The projectiles were approximately 0.2 g in mass and 5 mm in length with a 45° tip angle. The tip points were sufficiently sharp that they were not resolvable using optical microscopy, i.e. the tip diameter was less than $\sim 5 \mu\text{m}$. The tip diameters of all projectiles were checked using a confocal optical microscope (InfiniteFocus Optical Microscope, Alicona, Austria) prior to testing and any with a tip diameter greater than this value were rejected.

In order to compare the dynamic and quasi-static behaviour of the materials complementary tests were carried out at different strain rates. In dynamic tests a gas gun apparatus was used (Fig. 1) similar to that described in earlier work [11,12]. The sharpened projectiles described

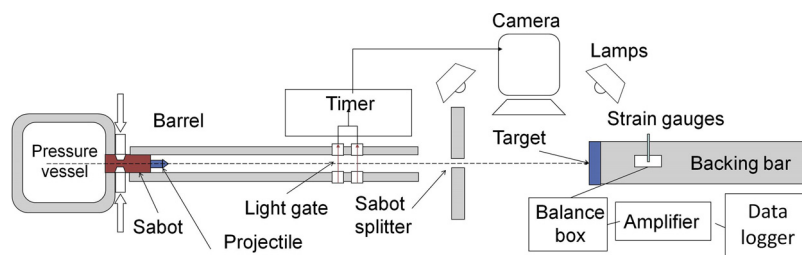


Fig. 1. Schematic diagram showing the dynamic impact test.

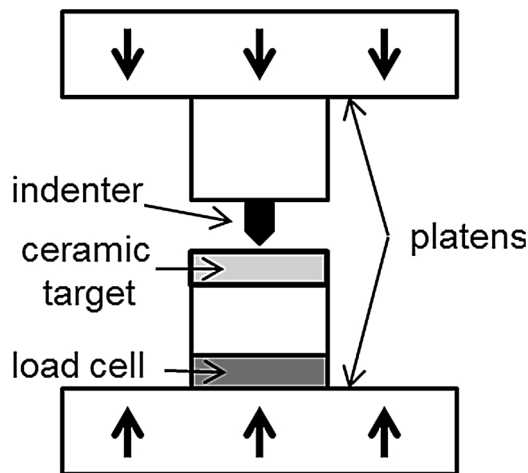


Fig. 2. Schematic diagram of the quasi-static test.

above were mounted to nylon sabots using double-sided tape and fired at ceramic targets of dimensions 25 mm diameter by 6 mm thickness mounted against a backing bar. The projectile and sabot were separated by means of a splitter. The load history was recorded using calibrated strain gauges mounted on the backing bar. The tests were filmed using a Phantom 7.1 High Speed Video Camera (Vision Research, USA) to confirm that the test was carried out successfully. The projectile speeds were measured at the light gates and from the images taken using the camera. Typically the velocity of the projectile measured at the light gates was around 250 m/s. Tests were carried out on two identically prepared discs of each material.

In quasi-static tests a projectile mounted in an aluminium holder was pushed against a ceramic disc using a 5582 Universal Testing System (Instron, USA) fitted with a 50 kN load cell operating in compression mode (Fig. 2). The displacement rate was 10 $\mu\text{m/s}$ and the motion was reversed when the load on the sample matched the maximum load experienced during the dynamic test (5.5 kN). The load and displacement were logged every 0.1 s using Bluehill Control Software (Instron, USA). Tests were carried out on three identically prepared discs of each material.

Following dynamic and static testing, discs were cleaned using acetone, and any residual steel from the projectile was removed by soaking in 16 M HCl solution for 5 min. The samples were examined using confocal optical microscopy (InfiniteFocus Optical Microscope, Alicona, Austria) to determine the depth and extent of the impact craters. The cracks and other damage in and around the impact craters were also examined using scanning electron microscopy (JEOL 840 F) on gold-coated samples.

Optical luminescence microscopy was carried out using a LabRAM ARAMIS Raman microscope (Jorbin Horiba, Japan) with a 633 nm red He-Ne laser and a Renishaw inVia Reflex Raman Microscope with a 633 nm red He-Ne laser and a 422 nm blue He-Cd laser. A 50x optical lens was used on both instruments. Line scans were obtained by

collecting spectra at points on lines passing through the impact site but including the undamaged region for comparison. By fitting the peaks in each spectrum using a pseudo-Voigt profile, the changes in position of the Cr^{3+} R1 fluorescence peak in alumina with position across the impact region were determined. All materials contained sufficient alumina that a Cr^{3+} fluorescence signal could be obtained, including the 3Y-TZP in which alumina was present as an impurity. For the hydrostatic stress state experienced by these samples, the residual stress is related to the change in wavenumber $\Delta\nu_{\text{R1}}$ of the R1 Cr^{3+} fluorescence peak from the zero stress condition by the following relationship:

$$\Delta\nu_{\text{R1}} = \Pi_H \sigma_H \quad (1)$$

where σ_H is the hydrostatic stress component and Π_H is the hydrostatic piezospectroscopic coefficient, taken as $7.59 \text{ cm}^{-1} \text{ GPa}^{-1}$ [28]. The position of the zero stress R1 peak was determined by averaging the results of 4 spectra taken near the edges of each specimen, far from the impacted or indented region.

In addition to the Cr^{3+} fluorescence spectroscopy using the 633 nm red laser, for zirconia-containing materials Raman spectra were also acquired using the 422 nm He-Cd laser to determine the relative quantities of tetragonal and monoclinic zirconia present inside and outside the impacted region. Line scans of spectra across the impact site were acquired using the Renishaw inVia Reflex Raman microscope as above. The relative proportion of monoclinic and tetragonal phases present was determined by using pseudo-Voigt peak fitting to obtain the relative areas of the monoclinic doublet at 181 and 190 cm^{-1} and the tetragonal peaks at 147 and 264 cm^{-1} . These peak areas were used to calculate the relative volume fraction of monoclinic zirconia present using the following equation [29,30]:

$$V_m = \frac{(I_m^{181} + I_m^{190})}{k(I_t^{147} + I_t^{267}) + I_m^{181} + I_m^{190}} \quad (2)$$

where k is a constant. This correcting factor has been determined by comparison against known standards to be $k = 0.33 \pm 0.03$ [29,30].

3. Results

3.1. Properties of ceramic materials

Samples of the materials supplied were examined by a number of characterisation methods to aid interpretation of dynamic and quasi-static impact and indentation test results. Their microstructures are shown in Fig. 3 and a summary of measured properties is given in Table 1.

The 3Y-TZP sample had a sub-micron grain size with a few larger grains ($> 3 \mu\text{m}$), usually interpreted as being cubic [22]. The debased alumina material contains large, blocky grains interspersed with a glassy matrix. The alumina-zirconia composite consisted of $\sim 2 \mu\text{m}$ alumina grains with smaller zirconia grains both in between and inside the alumina grains. The elastic properties reflected the major constituent of each material. The composite was the hardest material and the 3Y-TZP the strongest, by a significant margin.

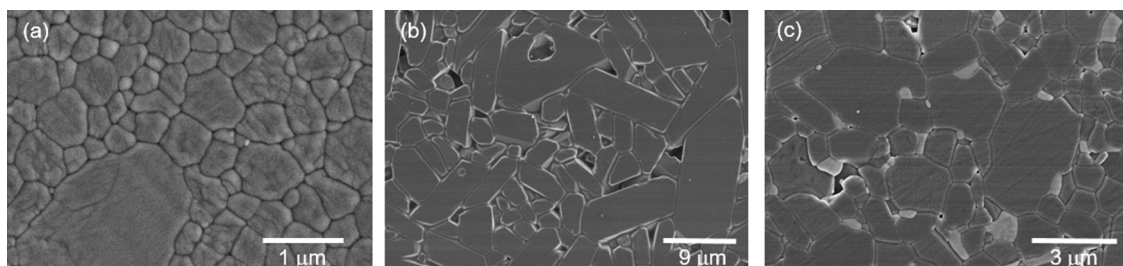


Fig. 3. SEM micrographs showing the microstructure of the materials. a) TZP, b) debased alumina, c) alumina-zirconia composite. Samples have been polished and thermally etched.

Table 1
Measured material properties of as-supplied samples.

Material	Density (g/cm ³)	Hardness (GPa)	Grain Size (μm)	Young's Modulus (GPa)	Shear Modulus (GPa)	Poisson's Ratio	Fracture Strength (MPa)
3Y-TZP	6.06 ± 0.01	12.8 ± 0.2	0.69 ± 0.07	213 ± 30	80.4 ± 3	0.33 ± 0.06	950 ± 100
Zirconia-Alumina Composite	4.06 ± 0.01	18.3 ± 0.5	1.9 ± 0.3	357 ± 50	142 ± 6	0.26 ± 0.04	360 ± 40
Debased Alumina	3.74 ± 0.01	12.5 ± 0.3	5.8 ± 0.9	330 ± 40	132 ± 6	0.25 ± 0.04	360 ± 30

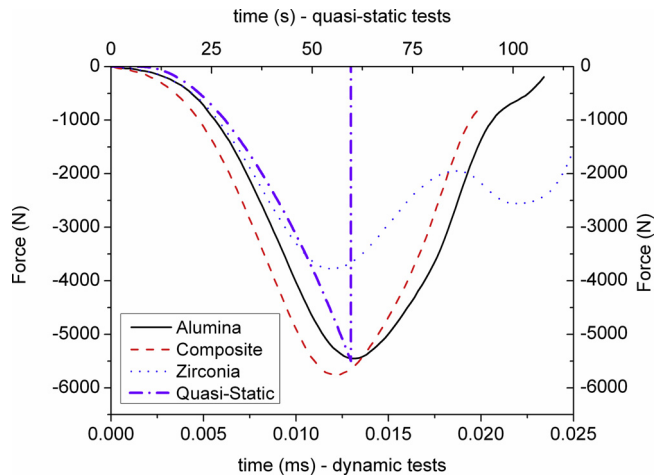


Fig. 4. Typical force-time curves for dynamic tests carried out on each material. A typical plot for a quasi-static test is also shown; note the different time axis scale for the dynamic and quasi-static tests.

3.2. Behaviour during dynamic impact and quasi-static indentation tests

Typical dynamic test force-time profiles recorded from the strain-gauged backing bar are shown in Fig. 4. Both the debased alumina and the composite material force-time profiles consist of a single compressive peak with a magnitude of approximately 5.5 kN. However the plots for the TZP samples have a double compressive peak, with a peak of around 3 kN occurring approximately 10 μs after the first peak of around 4 kN.

The quasi-static tests all had very similar force-time profiles as they primarily reflect the deformation of the projectile against the hard and stiff ceramics plates. One example is given in Fig. 4. The plot is non-linear owing to plasticity in the projectile tip, and has a sharp peak at the maximum load, at which point the testing machine was reversed.

Projectiles were recovered from quasi-static tests but could not usually be recovered from dynamic tests due to the set-up required to enable filming of the test, with one exception. The tip shape of the projectile which was retrieved was examined using confocal optical microscopy and compared to examinations of typical projectiles prior to testing and after being used for a quasi-static test (Fig. 5). In comparison to the initially sharp tip following testing the projectiles are significantly blunter after testing. The projectile from the quasi-static test has a blunted tip diameter around half that of the projectile recovered from the dynamic test. However as other dynamic test projectiles could not be recovered it is not possible to draw any general conclusions about the effect of different materials on the projectile blunting.

All dynamic tests were filmed using high-speed video to verify successful impact had occurred. The two samples of the same material generally showed similar behaviour and impact regions. In one test carried out on a TZP sample, a bright flash of light is observed just after impact of the projectile (Fig. 6). This phenomenon was not observed for other tests on TZP or other materials. Possible causes for this observation are discussed in Section 4.3 below.

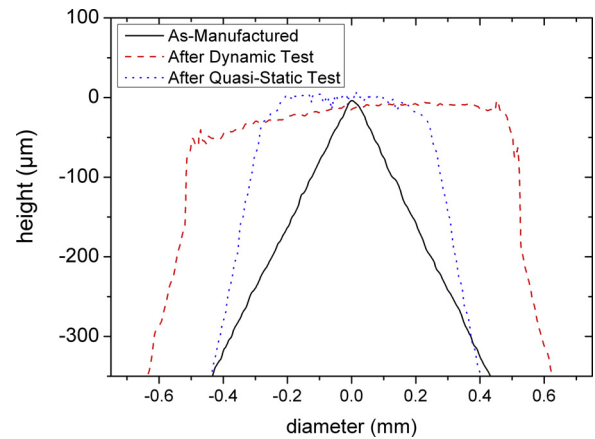


Fig. 5. Comparison of confocal optical microscope line profiles across the as-manufactured sharp projectile tip and the blunted tips of projectiles after use in the dynamic and quasi-static tests.

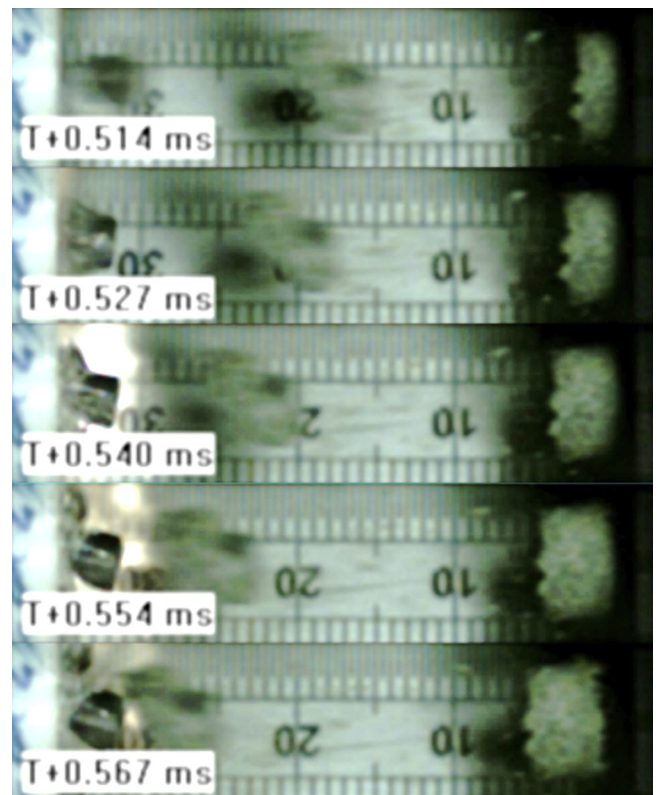


Fig. 6. High speed video images showing the observed flash of light during impact on a TZP sample.

3.3. Post-test characterisation

Profilometry line scans across the impacted regions measured using the confocal optical microscope show significant variation in the damage inflicted on each material by the quasi-static and dynamic tests

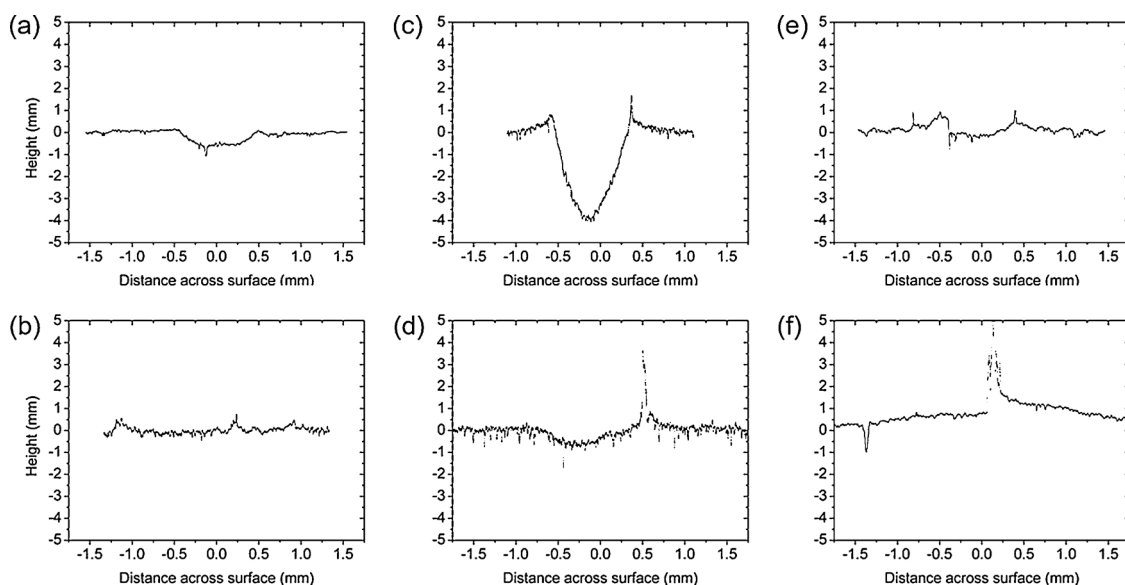


Fig. 7. Confocal optical profilometry of damaged regions in tested samples. Top row: Quasi-statically tested samples; bottom row: dynamically tested samples. (a,b) 3Y-TZP, (c,d) debased alumina, (e,f) alumina-zirconia composite. Sharp peaks in the spectra are due to debris on the surface which remained after cleaning with HCl.

(Fig. 7). In general for each material the impact craters were deeper for quasi-static tests than for dynamic tests. Repeated tests at each strain rate generated qualitatively similar damage for each set of identical samples. The extent of damage, assessed from the depth and width of the crater, is larger for the debased alumina samples than for the zirconia-containing materials.

Damaged regions in each material after quasi-static and dynamic tests were also examined in detail using low magnification optical microscopy and SEM. Some residual steel is observed in the sample surfaces (black regions in Fig. 8a–b, Fig. 9a–b, and Fig. 10a–b) despite cleaning with HCl. Damage to the zirconia-containing samples was less extensive and therefore more difficult to observe, particularly using optical microscopy where little cracking was observed (Figs. 8 and 10a–b). In the 3Y-TZP sample the impact region was only distinguishable from the rest of the sample by slight roughness and residual staining from the projectile but no micro- or macro-cracking could be observed by optical microscopy (Fig. 8) or in SEM (not shown).

The damage to the debased alumina samples (Fig. 9) was extensive and easily observed even using low magnification optical microscopy (Fig. 9c–d). In addition to multiple concentric ring cracks, around 10 radial surface cracks extending approximately 1 mm into the surrounding material were observed for the quasi-statically tested sample (Fig. 9c). Crack deflections were observed in these radial cracks (Fig. 9e) following the glass-crystal boundary before returning to the original direction. Either side of this deflection intragranular fracture is visible. While fewer radial cracks were observed for the dynamic tested

samples the cracks were significantly longer and resulted in greater loss of material (Fig. 9f). The ring cracks had smaller diameters for the quasi-statically tested samples (Fig. 9c) than for the dynamically tested samples (Fig. 9d). The ring crack diameters were similar to the projectile blunted tip diameter for the corresponding projectiles (see Section 3.2), being larger for the dynamically tested samples than for the quasi-static test.

In the composite samples (Fig. 10), a single ring crack was observed using SEM on a dynamic tested sample and some cracking was observed inside this ring crack (Fig. 10d), however overall it should be noted that the levels of damage were significantly lower than for the debased alumina.

Cr^{3+} fluorescence measurements of R1 peak shift were converted to hydrostatic residual stresses using Eq. (1) and are shown in Fig. 11. The most striking difference between the materials is that the residual stress fields at the centre of the indentations in alumina-zirconia composite and quasi-statically tested 3Y-TZP are tensile (positive shift) (Fig. 11a–b) while that for the debased alumina samples is compressive (Fig. 11c–d). The residual stress in the impacted region has a larger magnitude (whether compressive or tensile) for the quasi-statically tested samples than for the dynamically tested samples. While damaged regions in the debased alumina and alumina-zirconia composite materials can be fairly easily observed from these plots, the data for the dynamically tested 3Y-TZP is more dispersed, with both tensile and compressive residual stresses measured (Fig. 11a–b). This is consistent with the visual observation that limited levels of damage were

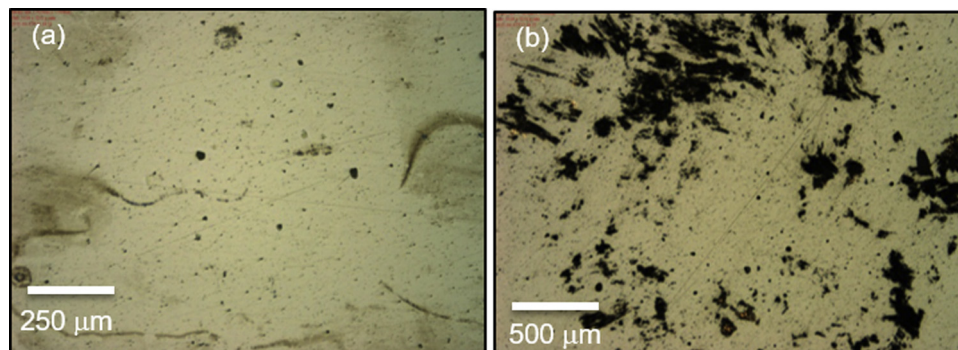


Fig. 8. Selected optical images of damaged regions in selected 3Y-TZP samples after (a) quasi-static testing and (b) dynamic testing.

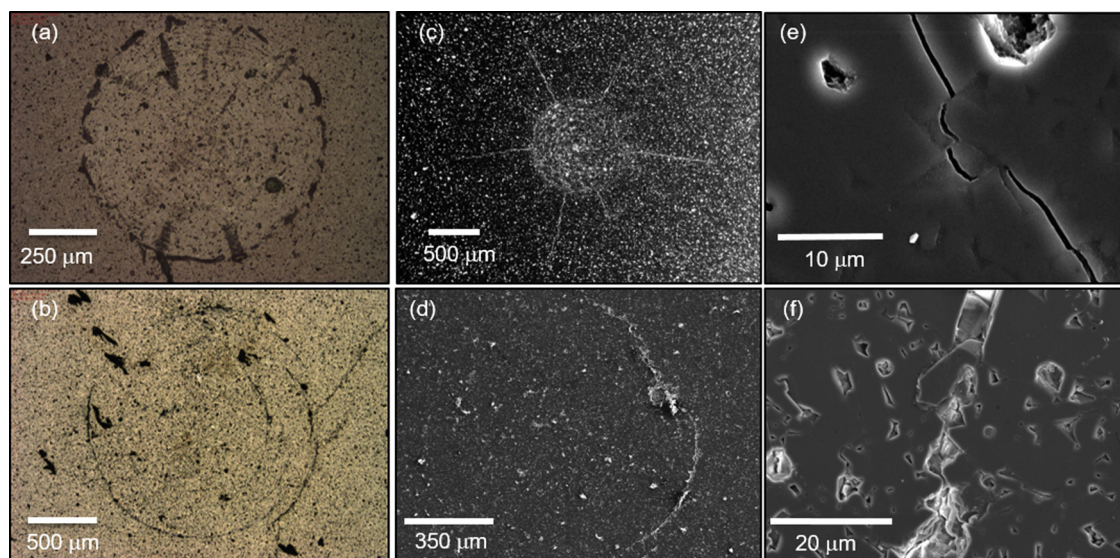


Fig. 9. Optical (a, b) and scanning electron microscopy (c–f) images of damaged regions in selected debased alumina samples after quasi-static testing (a, c, e) and dynamic testing (b, d, f). Note the different magnifications due to the varying scale of the defects observed.

sustained by this sample (Fig. 8).

The monoclinic ZrO_2 phase contents in the impacted or indented regions in the 3Y-TZP and alumina-zirconia composite samples were calculated using Eq. (2) using the measured tetragonal and monoclinic peak areas from Raman spectra acquired for Zr-containing samples. Fig. 12 shows the results of these calculations plotted as a function of position across the damaged site for the zirconia-alumina composite samples. It is clear that in the damaged regions of both quasi-statically and dynamically tested samples significantly elevated levels of monoclinic ZrO_2 are observed. Away from the impact site the monoclinic zirconia content of these samples was around 17 vol.% (dynamic) and 29 vol.% (quasi-static), which indicates that a significant increase in the monoclinic content to up to 93 vol.% (dynamic) and 98 vol.% (quasi-

static) has occurred in the damaged regions of the samples. In the quasi-static sample the damaged region has a higher average monoclinic ZrO_2 content than for the dynamically tested sample but across a narrower region. The width of the affected region is of the same order as that of the region of tensile residual stress observed in the Cr^{3+} fluorescence spectra (Fig. 11a–b).

The results for the Raman spectra taken from the 3Y-TZP samples are shown in Fig. 13. Unlike the zirconia-alumina composite, few spectra from the damaged region contained peaks due to monoclinic ZrO_2 , leading to the limited experimental data obtained. Monoclinic zirconia could not be detected in the 3Y-TZP samples before impact. As the detection limit for monoclinic zirconia using this method is lower than 10 vol.% [29] so it is clear that significantly less transformation as

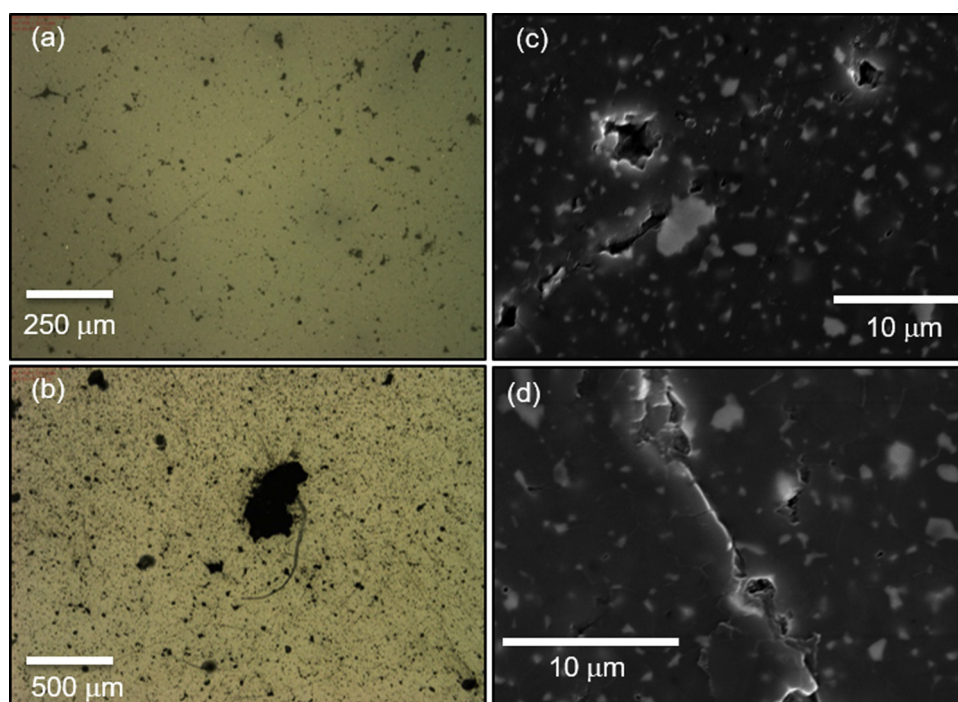


Fig. 10. Selected optical (a, b) and scanning electron microscopy (c, d) images of damaged regions in selected alumina-zirconia composite samples after quasi-static testing (a, c) and dynamic testing (b, d). Note the different magnifications due to the varying scale of the defects observed.

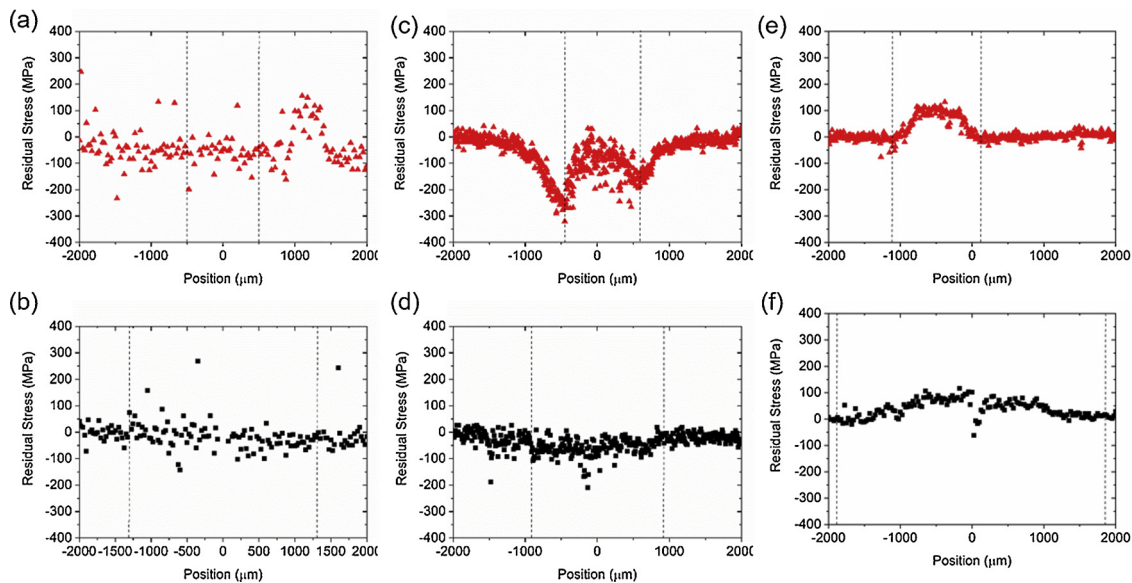


Fig. 11. Cr^{3+} fluorescence data linescans across the indented/impacted regions of the ceramic discs showing the distribution of residual stresses. Top row - quasi-statically tested samples; bottom row - dynamically tested samples. (a,b) 3Y-TZP, (c,d) debased alumina, (e,f) alumina-zirconia composite. Dashed vertical lines indicate the approximate region of damage on each sample.

a proportion of the zirconia present has occurred in the 3Y-TZP sample compared to the zirconia-alumina composites. As for the zirconia-alumina composite samples, peaks for monoclinic zirconia are observed over a large region of the surface for the dynamically-tested 3Y-TZP sample compared to the quasi-statically tested sample.

4. Discussion

4.1. Comparison of damage in the different ceramics

The debased alumina showed the most visible damage after testing (Figs. 7 and 9). Multiple ring cracks (associated with blunt indentation) were observed, along with radial cracks (associated with sharp indentation) originating from the ring-crack region [11]. The quasi-statically tested samples had shorter radial cracks which appeared to follow the grain boundaries quite closely. The radial cracks indicate some permanent deformation, probably associated with the glassy phase present in this material. The dynamically-tested samples by contrast had a smaller number of longer cracks which appeared wider as grains had been expelled from the cracked region. This difference probably stems from the greater blunting and hence longer range stresses of the projectile in the dynamic tests.

In the alumina-zirconia composite less damage was observed with only a single ring crack evident and no radial cracks (Fig. 10). The reduction in cracking is presumed to be a consequence of the higher hardness compared with the debased alumina, which leads to less

plastic deformation and therefore less radial cracking and more projectile blunting and therefore less ring cracking. No microcracking was observed and the levels of damage were fairly similar for the quasi-static and dynamically tested samples.

Overall the 3Y-TZP showed the most resistance to damage at both strain rates (Fig. 8), followed by the alumina-zirconia composite, and finally the debased alumina. The suppression of cracking can be explained in simple terms through the higher strength and toughness of this ceramic. This indicates that incorporating zirconia into alumina materials, or using 3Y-TZP if weight is not an issue, may result in armour with improved properties compared to pure alumina while still retaining the processing advantages of oxide-based materials.

4.2. Projectile deformation

The diameter of the blunted tip of the projectile following the dynamic test was approximately twice that in the equivalent quasi-static test (see Fig. 5). This can be simply explained in terms of the heating associated with plastic deformation. In quasi-static heating where the test is slow there is time for, the excess thermal energy to be conducted away from the tip region, so the effect of the heating is only observed during dynamic testing which occurs over a much shorter timescale. The blunting can be modelled by considering the deformation of the projectile tip from a sharp point to a blunt cylinder during the test. The derivation of the model is given in the Appendix. This model calculates a temperature change due to the deformation of 444 K.

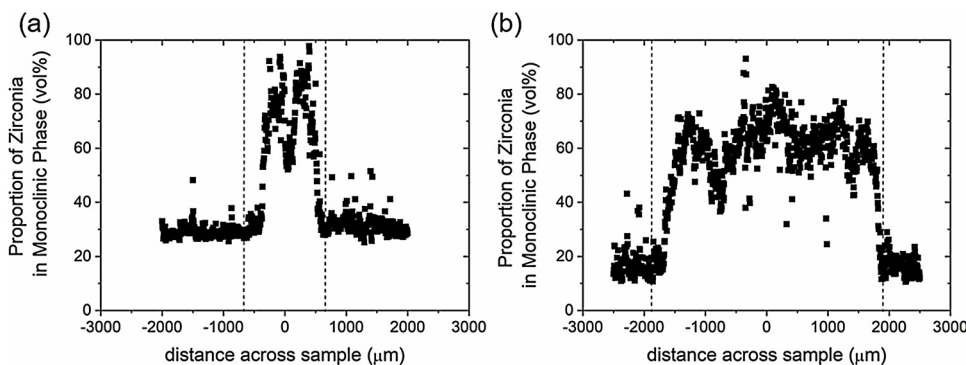


Fig. 12. Volume fraction of monoclinic phase (as a proportion of the total zirconia content only) varying with distance across damaged regions for the alumina-zirconia composite samples. (a) Quasi-statically tested sample, (b) dynamically tested sample. Values were calculated using Eq. (2) from peak areas measured from Raman spectra. Dashed vertical lines indicate the approximate region of damage on each sample.

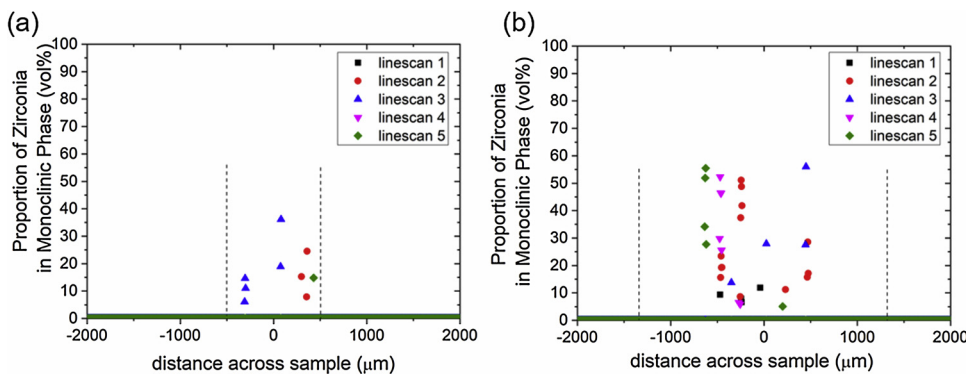


Fig. 13. Volume fraction of monoclinic phase varying with position across damaged regions for the 3Y-TZP samples as measured from Raman spectra (a) quasi-statically tested sample, (b) dynamically tested sample. Due to the limited number of spectra containing monoclinic peaks, five line scans were taken for each sample with 50 μm spacings between each line. Spectra from each linescan are represented by different shaped and coloured points. Dashed vertical lines indicate the approximate region of damage on each sample.

This is an approximate value due to the assumptions made in the calculation but it does show that large temperature rises are likely in the projectile tip during impact. This must be considered when comparing the effects of quasi-static and dynamic testing as the thermal effects will lower the effective yield stress of the projectile material. The ceramic would therefore appear to be stronger during dynamic testing than during quasi-static testing, whereas the correct interpretation is that the projectile becomes weaker, blunting more, and hence causing lower levels of damage.

4.3. Physical origin of peaks in the force-time profile

The shape of the impact curve is noticeably different for the TZP samples compared to the composite and debased alumina samples, consisting of two peaks rather than one. In the case of the composite and debased alumina samples, the compressive peak can be considered as a simple balance between the plastic deformation of the projectile causing an increase in the force as the projectile blunts and hence the rising curve, and the elastic rebound of the projectile, which pushes the projectile away from the surface of the sample and hence accounts for the falling side of the peak.

In the case of TZP, Fig. 4 shows that the force-time curve has a lower peak value than for the other ceramics but stops the projectile by applying force for a longer duration. The stiffness of TZP is of the same order as that of debased alumina and shows little damage after the test, so this surprising behaviour must be attributed to the unique mechanical properties of TZP. We suggest that the initial high tensile stresses around the impact site trigger the tetragonal to monoclinic transformation, allowing considerable deformation which absorbs the initial impact. As the projectile comes to a halt, the force it exerts on the ceramic decreases and constraint from the untransformed material around the impact site in conjunction with the local temperature increase forces most of the monoclinic phase to transform back to the tetragonal polytype. The thermodynamic forces involved coupled with the time taken for the reversal to occur produce the second “kickback peak” seen in Fig. 4. Reverse transformation in TZP at room temperature has been seen previously [31] and this explanation is supported by the small amount of monoclinic zirconia seen in Fig. 13, despite the high forces involved. The low volume fraction of zirconia in the composite prevents it from producing the same effect.

The same super-elastic cycle is assumed to have occurred in the quasi static tests as well but since the displacement in the unloading part of the tests was dominated by the elastic compliance of the testing machine, no effect was observed in the load vs. displacement curves.

The transformation may also be associated with the capture in the high-speed video images of one test on this material of a flash of light during the impact of the projectile (Fig. 6). This may simply be sparking of the steel projectile as it impacts the target but could also be mechanoluminescence, which is well known anecdotally to occur during grinding or sawing of TZP and has recently been investigated in more detail [32]. It is also known to occur in Ti-doped monoclinic zirconia

[33,34] though the mechanisms involved are yet to be identified.

The compressive residual stresses around the impact site in the debased alumina are similar to those observed previously [11,12] and result from limited plastic deformation under the impact site. Although the overall hardness of the debased alumina in the present case is much greater than the yield stress of the projectile, the glassy phase is much softer and allowed sufficient deformation to produce the relatively modest stresses measured here.

The tensile stresses seen in the zirconia-containing materials (Fig. 11) can be explained when it is considered that the Cr^{3+} fluorescence measurements probe only the alumina in the specimens. Both the composite and the TZP contain some transformed monoclinic zirconia and this would be heavily under compression owing to the $\sim 4\%$ expansion associated with the transformation. It follows that the remaining material, including the alumina, would be under tension to maintain the balance of forces.

This is consistent with the fact that in the zirconia-alumina composite samples, the region in which a tensile residual stress was measured by Cr^{3+} fluorescence from the alumina also contains the transformed monoclinic zirconia. In addition the quasi-statically tested zirconia-alumina composite sample, which had a higher tensile residual stress across a smaller area, showed higher volume fractions of monoclinic zirconia within that same area compared to the dynamically tested sample, where in both cases peak values were lower but the effect spread over a wider region owing to the greater blunting of the sample. Similar measurements by Huang et al. [35] on the residual stress in Vickers indentations in ZTA samples indicated that residual stress inside the indentation region is compressive. However, the degrees of plastic deformation and constraint and hence the indentation-induced stress levels are much greater for Vickers indentations than for the present impact sites and therefore masked the effect of the zirconia transformation.

While the proportion of the zirconia remaining in the transformed, monoclinic phase was significantly lower in the TZP than in the composite, it is important to account for the differences in zirconia content between the two materials. The 3Y-TZP samples were almost 100% $\text{Y}_2\text{O}_3\text{-ZrO}_2$ solid solution with a small amount of alumina impurity. The zirconia-alumina composites, by contrast, contained approximately 6.8 vol.% zirconia, with the balance being alumina. Therefore while a significantly greater proportion of the zirconia has transformed in the zirconia-alumina composites, the actual volume of material undergoing the transformation in each case may not be significantly different, perhaps restricted due to the orientation of grains relative to the surface, as observed by Deville et al. [36]. This, and the greater stiffness of the alumina matrix surrounding the transformed material in the composite may account for the higher tensile stresses it contained (Fig. 11).

5. Conclusions

Tests designed to directly compare the effects of indentation at different strain rates have been carried out on three ceramic materials

using a sharpened rod of hardened steel as the indenter/projectile. Of the materials tested, 3Y-TZP displayed the best resistance to impact, followed by alumina-zirconia composite and then the debased alumina. This ranking was determined by comparing the results of measurements of residual stress, extent and nature of cracking in the surface, and the size and depth of the damaged zone.

Materials displayed better resistance to impact when tested dynamically than when tested quasi-statically. This can be accounted for by considering the effects of heating of the projectile which results in changes to the projectile during the test, limiting the damage caused. This indicates that potential changes to the projectile must be considered when comparing the apparent strength of ceramic materials measured by similar tests.

The superior performance of the 3Y-TZP to damage during these tests was attributed to reversible transformation of tetragonal zirconia to the monoclinic phase during the test. This is assumed to explain the “double peak” shape of the dynamic impact test force-time curve, in which the momentum of the impact was absorbed over a longer period, reducing the maximum force and the extent of the damage. This behaviour was not observed in the alumina-zirconia composite material, which was attributed to the low tetragonal zirconia content of the material used in this work. However a composite with a higher tetragonal zirconia content may be suitable for use as an armour material

which combines the lower density of alumina or a carbide material with the superior mechanical properties of zirconia, and this will be the subject of future research.

Acknowledgements

The authors would like to thank Chris Hampson of Morgan Technical Ceramics for the provision of the materials studied in this work. We also thank Dr Geoff West, Prof. Clive Siviour, Dr Euan Wielewski, Dr Robert Paynter, Dr Igor Dyson, Dr Andrew Norton, Richard Duffin, Dick Froud, Laurie Walton, and Bob Lloyd for their help and advice. This study was carried out as part of the Understanding and Improving Ceramic Armour (UNICAM) project, jointly funded by the EPSRC (Grant Number EP/G042675/1) and DSTL United Kingdom Defence Science and Technology Laboratory. CEJD would also like to acknowledge EPSRC grant EP/R029873/1 for funding the work carried out at Warwick. The Renishaw inVia Reflex Raman Microscope used in this research was obtained through “Birmingham Science City: Innovative Uses for Advanced Materials in the Modern World” with support from Advantage West Midlands (AWM) and part funded by the European Regional Development Fund (ERDF).

Data published in this article can be freely downloaded from <http://wrap.warwick.ac.uk/120450>.

Appendix A

Derivation of the temperature change involved in the deformation of the projectile as stated in Section 4.2. The projectile shape changes during impact as shown in Fig. 5, which is represented mathematically as in the schematic Fig. A1 below.

From the assumed geometry shown in Fig. A1 above:

$$\pi r_2^2 b = \frac{1}{3} \pi r_2^2 (a + b) \quad (\text{A.1})$$

$$\therefore a = 2b \quad (\text{A.2})$$

where a , r_2 and b are the dimensions of the deforming parts of the projectile as shown in Fig. A1. It is also evident that:

$$r_2 = (a + b) \tan \theta = \frac{3}{2} a \tan \theta \quad (\text{A.3})$$

Assuming a mean yield stress σ_y the plastic work done in blunting the end is:

$$\int_0^a \pi r_2^2 \sigma_y da = \int_0^{r_2} \frac{2\pi}{3 \tan \theta} \sigma_y r_2^2 dr_2 = \frac{2\pi}{9 \tan \theta} \sigma_y r_2^3 \quad (\text{A.4})$$

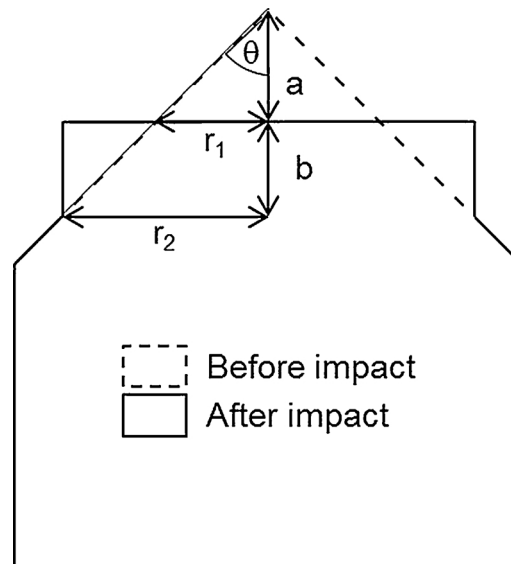


Fig. A1. Schematic diagram of the deformations considered in analysing the projectile tip shape changes during quasi-static and dynamic testing. a and r_1 are the height and base radius of the cone-shaped tip of the projectile which is flattened during the test. b and r_2 are the height and radius of the blunt end of the projectile resulting from this deformation.

Assuming uniform and adiabatic heating of the deformed material, and substituting using the geometric relationships in Eqs. (A.2) and (A.3), the temperature rise ΔT is:

$$\Delta T = \frac{2\pi}{9 \tan \theta} \frac{\sigma_y r_2^3}{c \rho \pi r_2^2 b} = \frac{2\sigma_y}{3c\rho} \quad (\text{A.5})$$

where c is the heat capacity and ρ is the density of the steel projectile material. It can be assumed that 90% of the work done becomes heat (after Rogers [37]) and that all of the heat remains in the deformed region throughout the deformation time and so gives an increase in temperature. For the steel used for the projectile $c = 490 \text{ J kg}^{-1} \text{ K}^{-1}$ and $\rho = 8000 \text{ kg m}^{-3}$, and the mean yield stress σ_y of 2.9 GPa can be assessed using the relationship that Vickers hardness is approximately $3\sigma_y$ for metals (as measured in Section 2 as 8.6 GPa). Therefore from Eq. A.5 ΔT is calculated to be 444 K.

References

- [1] S.M. Walley, Historical review of high strain rate and shock properties of ceramics relevant to their application in armour, *Adv. Appl. Ceram.* 109 (2010) 446–466, <https://doi.org/10.1179/174367609X422180>.
- [2] J.C. LaSalvia, J. Campbell, J.J. Swab, J.W. McCauley, Beyond hardness: ceramics and ceramic-based composites for protection, *J. Mater.* 62 (2010) 16–23.
- [3] I.G. Crouch, Body armour - New materials, new systems, *Def. Technol.* 15 (2019) 241–253, <https://doi.org/10.1016/j.dt.2019.02.002>.
- [4] A. Healey, J. Cotton, S. MacLachlan, P. Smith, J. Yeomans, Understanding the ballistic event: methodology and initial observations, *J. Mater. Sci.* 52 (2017) 3074–3085, <https://doi.org/10.1007/s10853-016-0594-0>.
- [5] J. Lankford, Mechanisms responsible for strain-rate-dependent compressive strength in ceramic materials, *J. Am. Ceram. Soc.* 64 (1981) C33–C34.
- [6] J. Lankford, High strain rate compression and plastic flow of ceramics, *J. Mater. Sci. Lett.* 15 (1996) 745–750, <https://doi.org/10.1007/BF00274593>.
- [7] S.K. Chung, Fracture characterization of armor ceramics, *Am. Ceram. Soc. Bull.* 69 (1990) 358–366.
- [8] J. Sternberg, Material properties determining the resistance of ceramics to high velocity penetration, *J. Appl. Phys.* 65 (1989) 3417, <https://doi.org/10.1063/1.342659>.
- [9] N.K. Bourne, J.C.F. Millett, M. Chen, J.W. McCauley, D.P. Dandekar, On the Hugoniot elastic limit in polycrystalline alumina, *J. Appl. Phys.* 102 (2007) 073514, <https://doi.org/10.1063/1.2787154>.
- [10] D.E. Munson, R.J. Lawrence, Dynamic deformation of polycrystalline alumina, *J. Appl. Phys.* 50 (1979) 6272–6282.
- [11] C.E.J. Dancer, H.M. Curtis, S.M. Bennett, N. Petrinic, R.I. Todd, High strain rate indentation-induced deformation in alumina ceramics measured by Cr³⁺ fluorescence mapping, *J. Eur. Ceram. Soc.* 31 (2011) 2177–2187, <https://doi.org/10.1016/j.jeurceramsoc.2011.06.002>.
- [12] C.E.J. Dancer, H.M. Curtis, S.M. Bennett, N. Petrinic, R.I. Todd, Measurement of deformation in alumina samples indented at high strain rates, *Ceram. Eng. Sci. Proc.* 32 (2011) 227–236.
- [13] B. Lawn, R. Wilshaw, Indentation fracture: principles and applications, *J. Mater. Sci.* 10 (1975) 1049–1081, <https://doi.org/10.1007/BF00823224>.
- [14] P.J. Hazell, *Ceramic Armour: Design and Defeat Mechanisms*, Argos Press, 2006.
- [15] E. Medvedovski, Alumina ceramics for ballistic protection part I, *Am. Ceram. Soc. Bull.* 81 (2002) 27–32.
- [16] W.W. Chen, A.M. Rajendran, B. Song, X. Nie, Dynamic fracture of ceramics in armor applications, *J. Am. Ceram. Soc.* 90 (2007) 1005–1018, <https://doi.org/10.1111/j.1551-2916.2007.01515.x>.
- [17] P. Forquin, G. Rossiquet, J. Zinsner, B. Erzar, Microstructure influence on the fragmentation properties of dense silicon carbides under impact, *Mech. Mater.* 123 (2018) 59–76, <https://doi.org/10.1016/j.mechmat.2018.03.007>.
- [18] B. Koepfel, G. Subhash, Characteristics of residual plastic zone under static and dynamic Vickers indentations, *Wear* 224 (1999) 56–67, [https://doi.org/10.1016/S0043-1648\(98\)00328-7](https://doi.org/10.1016/S0043-1648(98)00328-7).
- [19] R.J. Anton, G. Subhash, Dynamic Vickers indentation of brittle materials, *Wear* 239 (2000) 27–35.
- [20] G. Subhash, Dynamic indentation testing, *ASM Handb. Vol. 8 Mech. Test. ASM*, 2000, pp. 519–529.
- [21] R.C. Garvie, R.H. Hannink, R.T. Pascoe, Ceramic Steel? *Nature* 258 (1975) 703–704.
- [22] R.H.J. Hannink, P.M. Kelly, B.C. Muddle, Transformation toughening in zirconia-containing ceramics, *J. Am. Ceram. Soc.* 83 (2000) 461–487.
- [23] C. Huang, Y. Chen, Effect of varied alumina / zirconia content on ballistic performance of a functionally graded material, *Int. J. Refract. Metals Hard Mater.* 67 (2017) 129–140, <https://doi.org/10.1016/j.ijrmhm.2017.04.002>.
- [24] G.R. Anstis, P. Chantikul, B.R. Lawn, D.B. Marshall, A critical evaluation of indentation techniques for measuring fracture toughness: I, direct crack measurements, *J. Am. Ceram. Soc.* 64 (1981) 533–538.
- [25] Advanced Technical Ceramics — Mechanical Properties of Monolithic Ceramics at Room Temperature — Part I: Determination of Flexural Strength, (2006), p. 3.
- [26] Advanced technical ceramics — Mechanical Properties of Monolithic Ceramics at Room Temperature — Part 2: Determination of Young's modulus, Shear Modulus and Poisson's Ratio, (2006), pp. 1–40 Vol. 3.
- [27] M.I. Mendelson, Average grain size in polycrystalline ceramics, *J. Am. Ceram. Soc.* 52 (1969) 443–446, <https://doi.org/10.1111/j.1151-2916.1969.tb11975.x>.
- [28] J. He, D.R. Clarke, Determination of the piezospectroscopic coefficients for chromium-doped sapphire, *J. Am. Ceram. Soc.* 78 (1995) 1347–1353.
- [29] J.A. Muñoz Tabares, M.J. Anglada, Quantitative analysis of monoclinic phase in 3Y-TZP by Raman spectroscopy, *J. Am. Ceram. Soc.* 93 (2010) 1790–1795, <https://doi.org/10.1111/j.1551-2916.2010.03635.x>.
- [30] C.S. Lim, T.R. Finlayson, F. Ninio, J.R. Griffiths, In-situ measurement of the stress-induced phase transformations in magnesia-partially-stabilized zirconia using Raman spectroscopy, *J. Am. Ceram. Soc.* 75 (1992) 1570–1573.
- [31] M. Saran, *Strengthening of Zirconia at High Temperatures*, University of Oxford, 2008.
- [32] K. Wang, L. Ma, X. Xu, S. Wen, Y. Zhang, Enhancement of triboluminescence in the presence of CO < inf > 2 < /inf > by sliding between silica and yttria-stabilized zirconia, *Langmuir* 31 (2015) 8224–8227, <https://doi.org/10.1021/acs.langmuir.5b01335>.
- [33] M. Akiyama, C.-N. Xu, K. Nonaka, Intense visible light emission from stress-activated ZrO₂:Ti, *Appl. Phys. Lett.* 81 (2002) 457, <https://doi.org/10.1063/1.1494463>.
- [34] B.P. Chandra, Persistent mechanoluminescence induced by elastic deformation of ZrO₂:Ti phosphors, *J. Lumin.* 130 (2010) 2218–2222, <https://doi.org/10.1016/j.jlumin.2010.06.023>.
- [35] S. Huang, J.G.P.G.P. Binner, B. Vaidyanathan, R.I.I. Todd, Quantitative analysis of the residual stress and dislocation density distributions around indentations in alumina and zirconia toughened alumina (ZTA) ceramics, *J. Eur. Ceram. Soc.* 34 (2014) 753–763, <https://doi.org/10.1016/j.jeurceramsoc.2013.09.021>.
- [36] S. Deville, G. Guénin, J. Chevalier, Martensitic transformation in zirconia Part I. Nanometer scale prediction and measurement of transformation induced relief, *Acta Mater.* 52 (2004) 5697–5707, <https://doi.org/10.1016/j.actamat.2004.08.034>.
- [37] H.C. Rogers, Adiabatic plastic deformation, *Annu. Rev. Mater. Sci.* 9 (1979) 283–311, <https://doi.org/10.1146/annurev.ms.09.080179.001435>.